

## Ensemble Monte Carlo simulation of intervalley scattering in $\text{Al}_x\text{Ga}_{1-x}\text{As}$

Selim E. Günger and David K. Ferry

Center for Solid State Electronics Research, Arizona State University, Tempe, Arizona 85287-6206

(Received 29 May 1992)

An ensemble Monte Carlo simulation of the femtosecond response of photoexcited electrons in indirect-gap  $\text{Al}_x\text{Ga}_{1-x}\text{As}$  is performed. The time evolution of electron populations in the conduction-band valleys is studied. By comparing with recent femtosecond infrared-absorption experiments, a value for the  $L$ - $X$  intervalley deformation potential was derived through parameter fitting. The effect of binary phonon modes due to the alloy structure of the semiconductor is incorporated into the simulation of both the ultrafast scattering processes and the indirect photogeneration process. The value found for the  $L$ - $X$  intervalley deformation potential,  $D_{XL} = 1.7 \pm 0.5 \times 10^8$  eV/cm, can be assumed as a lower bound for the deformation potential in GaAs.

### I. INTRODUCTION

With the push for smaller device dimensions and higher-frequency operation, hot-electron phenomena, particularly ultrafast scattering processes in the femtosecond time range, have become an extensive area of research. A number of groups have been active in studying the intervalley scattering among the  $\Gamma$ ,  $L$ , and  $X$  valleys in GaAs,<sup>1-6</sup> which is one of the dominant scattering mechanisms for hot electrons with energies above the intervalley scattering threshold. Experimental techniques based on optical excitation measurements and transport are the basis for various determinations of the intervalley scattering parameters through a numerical parameter fit to measurements of population evolutions monitored by pulsed photoexcitation pump-probe techniques,<sup>1,5</sup> linewidth broadening of the photoluminescence spectra in continuous-wave optical excitation,<sup>2,3</sup> and mobility measurements.<sup>7,8</sup> Numerical simulations using ensemble Monte Carlo (EMC) techniques are generally employed for parameter fitting to such data, as well as rate-equation-based methods on pulsed<sup>5</sup> or continuous-wave photoexcitation.<sup>10</sup> Theoretical treatments of the intervalley scattering deformation potential using empirical pseudopotential methods have also been reported.<sup>11</sup> However, these various methods have resulted in a wide range of values for important intervalley scattering deformation potentials such as the  $\Gamma$ - $L$  deformation potential, which range over an order of magnitude as  $(1-10) \times 10^8$  eV/cm, and is a continuing matter of investigation, although the measurements and theory seem to be converging to an accepted  $7 \times 10^8$  eV/cm for this value.<sup>1,9,10</sup>

Relatively little work has been done to directly study the  $L$ - $X$  intervalley scattering process, the uncertainty of which also affects the determinations of the  $\Gamma$ - $L$  and  $\Gamma$ - $X$  intervalley scattering lifetimes. The scattering between the  $L$  and  $X$  valleys in GaAs has mostly been treated through a numerical fit to transport measurements.<sup>7,8</sup> Since GaAs is a direct-gap semiconductor, this process cannot be monitored directly by optical techniques. Recent femtosecond-scale infrared-absorption measurements of Wang *et al.*<sup>12</sup> provide access to the measure-

ment of this scattering process in indirect-gap  $\text{Al}_{0.6}\text{Ga}_{0.4}\text{As}$ . These latter authors obtain a value for the  $L$ - $X$  intervalley scattering lifetime and deformation potential from a rate-equation analysis. This value of the scattering lifetime can be used to set an "upper bound" for the  $X$ - $L$  intervalley scattering time constant for GaAs, since the density-of-states mass for the  $X$  valley in GaAs is greater than in  $\text{Al}_x\text{Ga}_{1-x}\text{As}$ .<sup>12</sup> However, it should be noted that estimates of lifetimes are notably poor estimates of actual scattering rates.<sup>13</sup>

In this study, we have developed a three-valley EMC simulation for the photoexcitation and relaxation of electrons in the various conduction bands of indirect-gap  $\text{Al}_{0.6}\text{Ga}_{0.4}\text{As}$ . The  $L$ - $X$  intervalley deformation potential is determined by parameter fitting to the femtosecond time-resolved absorption data of Ref. 12.

### II. SIMULATION

The band-structure picture we use to study intervalley scattering of electrons in indirect-gap  $\text{Al}_{0.6}\text{Ga}_{0.4}\text{As}$  is shown in Fig. 1. Electrons in the valence band are directly excited to the conduction-band valleys ( $X$  and  $L$ ) using a 400-fs full width at half maximum (FWHM), 212-eV pulse beam with a photoexcitation density of  $n = 2.8 \times 10^{18}$   $\text{cm}^{-3}$ . The absorption process is an in-

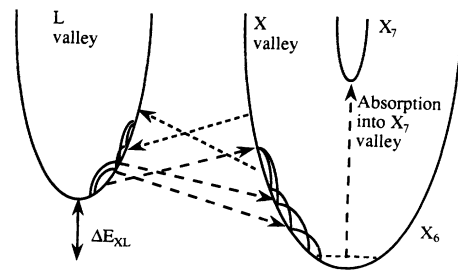


FIG. 1. Band-structure schematic of  $\text{Al}_x\text{Ga}_{1-x}\text{As}$  showing the intervalley and intravalley phonon-scattering processes and the  $X_6$ - $X_7$  intervalley infrared-absorption transition.

direct one, and involves intervalley phonons, a point that plays a major role in the simulation, as discussed below. The conduction-band carriers undergo elastic- (acoustic-phonon) and inelastic- (polar-optical-phonon, intervalley and intravalley optical-phonon deformation-potential scattering) scattering events at room temperature, and accumulate at the bottom of the  $X_6$  valley. This population is probed through the absorption of a 3.3- $\mu\text{m}$ , 500 fs infrared pulse which excites these carriers to the  $X_7$  valley. Because the infrared probe pulse has a similar time resolution to the excitation pulse, these effects are convolved in time, and the simulation must account for this convolution as well.

#### A. Material parameters and scattering rates

We have used the bulk material parameters for  $\text{Al}_x\text{Ga}_{1-x}\text{As}$  for the band structure near the  $\Gamma$ ,  $X$ , and  $L$  points, and the effective masses in these valleys, of Adachi<sup>14</sup> (see Table I). The virtual-crystal approximation, i.e., the interpolation of the constituent material (GaAs and AlAs) values for a given composition  $x$  with relevant bowing parameters, was avoided wherever solid experimental data were available in the literature. A parabolic band approximation for the lower-lying  $X$  and  $L$  valleys was assumed, while nonparabolicity for the  $\Gamma$  valley was considered in the calculations of scattering rates and energy-momentum relations.

Electron-phonon interactions in the ternary allow  $\text{Al}_x\text{Ga}_{1-x}\text{As}$  are greatly influenced by the fact that the lattice structure supports two distinct sets of LA, TA, LO, and TO modes due to the GaAs-like lattice interweaved with the AlAs-like lattice.<sup>15</sup> We consider that both sets of modes will contribute to the indirect-gap generation of electrons into the conduction-band valleys. The scattering from both types of phonons is also taken into consideration for polar optical and nonpolar intervalley and intravalley scattering. The phonon strength ratios, i.e., the partitioning of the total phonon power into the AlAs-like and GaAs-like sets, are found in Raman-scattering measurements,<sup>15</sup> which depict approximately a one-to-one ratio of phonon strengths for  $x=0.6$ . The zone-center phonon energies  $\hbar\omega_{\text{LO}}$  for  $x=0.6$  in  $\text{Al}_x\text{Ga}_{1-x}\text{As}$  are found from these same data. However,

the zone-edge phonon energies, which are involved in intervalley and intravalley scattering, are found to be fairly broad experimentally, so the values used were obtained through a linear interpolation of their constituent material values and are assumed equal for both the  $X$  and  $L$  points. This fit is easily within the broadness of the observed Raman lines. The scattering due to each of the two modes is treated as if it were a different scattering process. Thus we have scattering by one phonon with an AlAs-like zone-edge phonon energy, and by a second with a GaAs-like zone-edge phonon energy. A relevant partitioning of the phonon strength is made, based upon the relative Raman strengths, but the same density-of-states parameters are used, as these latter measure the number of final states for the scattering process. For optical-phonon scattering in III-V semiconductors selection rules from symmetry considerations allow only certain phonon modes to take part in intervalley and intravalley scattering. The nonpolar optical deformation-potential scattering rate expression for zero-order scattering can be written as<sup>16</sup>

$$\frac{1}{\tau_{\text{scat}}} = N_v \frac{(m^*)^{3/2} D^2}{\sqrt{2\pi\rho\hbar^3}\omega_0} [N_q + \frac{1}{2} \pm \frac{1}{2}] \sqrt{E - \Delta E \mp \hbar\omega_0}, \quad (1)$$

where  $N_v$  is the number of valleys to which the initial state can scatter, namely one for intravalley scattering and scattering to the  $\Gamma$  valley, four for scattering into the  $L$  valley, and three for scattering into the  $X$  valley,  $m^*$  is the density-of-states mass of the final state,  $D$  is the nonpolar optical deformation potential for the allowed phonon mode,  $N_q$  is the phonon occupation number,  $\Delta E$  is the difference between the band minima of the initial and final state,  $\rho$  is the mass density, and  $\omega_0$  is the phonon frequency. The  $+$  and  $-$  signs in the phonon occupation factor refer to the cases of phonon emission and absorption, respectively. Where zero-order phonon-scattering processes are forbidden from symmetry considerations, first-order corrections to optical deformation-potential scattering can be made:<sup>16</sup>

$$\frac{1}{\tau_{\text{scat}}} = N_v \frac{\sqrt{2}(m^*)^{5/2}\Xi_0^2}{\pi\rho\hbar^5\omega_0} [(N_q + \frac{1}{2} \pm \frac{1}{2})] \times [2E - (\Delta E \pm \hbar\omega_0)] \sqrt{E - (\Delta E \pm \hbar\omega_0)}, \quad (2)$$

TABLE I.  $\text{Al}_{0.6}\text{Ga}_{0.4}\text{As}$  material parameters.

$m_x$	0.368( $m_0$ )	$\omega_{\text{BZ}}(\text{GaAs})$	0.0273 eV
$m_L$	0.246	$\omega_{\text{BZ}}(\text{AlAs})$	0.045 eV
$m_\Gamma$	0.1168	$\omega_{\text{LA}}(\text{GaAs})$	0.012 eV
$m_{\text{hh}}$	0.704	$\omega_{\text{LA}}(\text{AlAs})$	0.015
$m_{\text{lh}}$	0.1248	$D_{\Gamma L}$	$7.0 \times 10^8$ eV/cm
$m_{X7}$	0.070	$D_{XL}$	$1.5 \times 10^8$ eV/cm
$E_{\text{gap}}$	2.0203 eV	$D_{XX}, D_{LL}, D_{X\Gamma}$	$1.0 \times 10^9$ eV/cm
$\Delta E_{XL}$	0.066 eV	$\epsilon(0)$	$9.25(\epsilon_0)$
$\Delta E_{X\Gamma}$	0.1715 eV	$\epsilon_{\text{int}}$	10.00
$\Delta E_{L\Gamma}$	0.1048 eV	$\epsilon_\infty$	11.31
$\Delta E_{X6-X7}$	0.300 eV	$\Xi_0$	5.0 eV
$\omega_{\text{LO}}(\text{GaAs})$	0.033 eV	$\Xi_1$	7.0 eV
$\omega_{\text{LO}}(\text{AlAs})$	0.049 eV	$\rho$	$4400 \text{ kg/m}^3$
$v_s$	5770 m/s		

where  $\Xi_0$  is the first-order optical coupling constant.

From selection rules,<sup>16,17</sup> the zero-order intravalley scattering within the  $\Gamma$  valley is not allowed. We have not included a first-order scattering correction to this case. Intravalley  $X$  scattering occurs through LA and TA phonons only, while intravalley  $L$  scattering involves all possible modes LA, LO, TA, and TO. Intervalley scattering selection rules for  $X$ - $X$  scattering (to different equivalent valleys) are due to LO phonons only, since the mass of the Ga and Al atoms are less than the As atom.  $L$ - $L$  intervalley scattering involves both longitudinal modes LA and LO. Intervalley  $L$ - $X$  scattering is due to the LO-phonon modes only. We include also a first-order scattering correction due to the LA modes for this case. The intervalley scattering between the  $\Gamma$  valley and the  $X$  and  $L$  valleys is due to the LO-phonon modes.

For polar-optical-phonon scattering, the existence of two LO modes due to GaAs-like and AlAs-like phonons shows itself by a modification of the Fröhlich coupling constant for each of the electron-polar-optical-phonon scattering interactions. For the case of a single LO phonon existing in the lattice, the dielectric constant for the long-wavelength case, excluding plasma effects, is given by the expression<sup>16</sup>

$$\epsilon(\omega) = \epsilon_\infty \left[ 1 + \frac{\omega_{LO}^2 - \omega_{TO}^2}{\omega_{TO}^2 - \omega^2} \right], \quad (3)$$

where  $\epsilon_\infty$  is the optical-frequency dielectric constant and  $\omega_{LO}$  and  $\omega_{TO}$  are the LO- and TO-phonon frequencies. The ionic polarization, which causes the electron-polar-optical-phonon interaction, is characterized by an effective charge with which the scattering electrons interact. Optical-frequency polarization, proportional to  $\epsilon_\infty^{-1}$ , does not have an ionic component since ionic motion cannot follow the high frequencies. Hence, the ionic polarization is identified through the Fröhlich coupling constant, given by

$$\Gamma = \omega_{LO}^2 \left[ \frac{1}{\epsilon_L} - \frac{1}{\epsilon_H} \right], \quad (4)$$

and is thereby purely of ionic origin. Here,  $\epsilon_H$  and  $\epsilon_L$  are the high- and low-frequency dielectric constants appropriate to the particular mode. The effective ionic charge is proportional to this Fröhlich constant, as a difference between the inverse of dielectric constants at frequency  $\omega > \omega_{LO} > \omega_{TO}$  and  $\omega < \omega_{TO}$ . When we have two TO modes as in  $Al_xGa_{1-x}As$ , the dielectric constant has two singularity points (see Fig. 2). We can distribute the total effective ionic charge between the two TO lines. For higher-frequency LO phonons, i.e., the AlAs-like LO phonon, the Fröhlich coupling constant is given by

$$\Gamma = \omega_{LO(AlAs)}^2 \left[ \frac{1}{\epsilon_{int}} - \frac{1}{\epsilon_\infty} \right]. \quad (5)$$

The remaining part of the effective ionic charge is due to the GaAs-like LO phonon, with Fröhlich constant

$$\Gamma = \omega_{LO(GaAs)}^2 \left[ \frac{1}{\epsilon(0)} - \frac{1}{\epsilon_{int}} \right]. \quad (6)$$

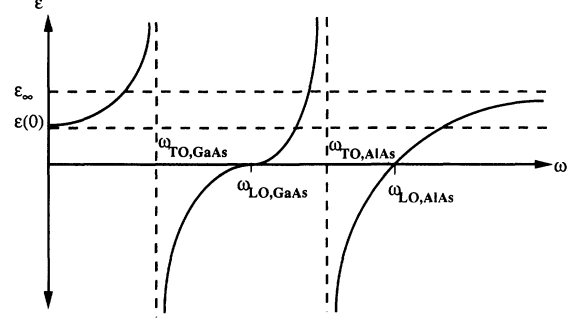


FIG. 2. Dielectric constant dispersion for the alloy modes. Two singularities due to the AlAs-like and GaAs-like phonons exist.

Here,  $\epsilon_{int}$  is an intermediate dielectric constant, whose value is to be determined.<sup>16,18</sup> The criterion for determining this is the fact that the phonon line strengths for long-wavelength LO phonons from the Raman-scattering spectra are approximately equal. Hence, by using the two Fröhlich constants given by (5) and (6), we have effectively partitioned the total polar-optical-phonon scattering process between the two LO modes. For this purpose, we have set  $\epsilon_{int} = 10\epsilon_0$ .

The polar-optical-phonon scattering is also influenced by the presence of other carriers through screening. Under the assumption of no screening, the polar-optical-phonon scattering rate is given by<sup>16</sup>

$$\frac{1}{\tau_{scat}} = \frac{m^* e^2 \omega_{LO}}{4\pi\hbar^2 k} \left[ \frac{1}{\epsilon_L} - \frac{1}{\epsilon_H} \right] \times \left\{ \left( Nq + \frac{1}{2} \pm \frac{1}{2} \right) \ln \left[ \frac{k + \sqrt{k^2 \mp q_0^2}}{\pm k + \sqrt{k^2 \mp q_0^2}} \right] \right\}, \quad (7)$$

where  $q_0$  is the phonon wave vector and  $k$  is the electron wave vector. We have implemented the effect of reduction of this scattering rate through screening through a random number rejection technique in the program, whereby the matrix element is reduced by a factor<sup>19</sup>

$$\Gamma \sim \omega_{LO}^2 \left[ \frac{1}{\epsilon_L} - \frac{1}{\epsilon_H} \right] \frac{q^4}{(q^2 + \beta^2)^2}. \quad (8)$$

An important characteristic is that the Debye screening length can be a time-dependent quantity. Following the approach of Osman and Ferry,<sup>20</sup> the time-dependent screening wave vector  $\beta$  was calculated at each time step as (for parabolic bands)

$$\beta^2 = \frac{ne^2}{\epsilon_s} \frac{1}{N} \sum_i \frac{1}{2E_i}, \quad (9)$$

where  $n$  is the electron concentration,  $N$  is the number of electrons in the simulation,  $E_i$  is the energy of electron  $i$ ,  $\epsilon_s$  is the static dielectric constant, and the summation runs over all electrons in the simulation. For nonparabolic bands, the expression for the screening wave vector

can be modified as<sup>20</sup>

$$\beta^2 = \frac{ne^2}{\epsilon_s} \frac{1}{N} \sum_i \left\{ \frac{2\alpha}{1+2\alpha E_i} + \frac{1+2\alpha E_i}{2E_i(1+\alpha E_i)} \right\}, \quad (10)$$

where  $\alpha$  is the nonparabolicity factor. Hence, by recalculating only the screening wave vector  $\beta$  at each time step and reducing the scattering rate through a rejection technique, we do not have to calculate the polar-optical-phonon scattering rates at each time step.

Acoustic-phonon scattering is also treated. The existence of alloy phonon modes does not have any effect on this scattering process. The scattering rate is given by

$$\frac{1}{\tau_{\text{scat}}} = \frac{\Xi_1^2 k_B T (2m^*)^{3/2}}{2\pi \hbar^4 \rho v_s^2} E^{1/2}, \quad (11)$$

where  $\Xi_1^2$  is the acoustic deformation potential and  $v_s$  is the velocity of sound.

The scattering rates given so far assume nondegenerate statistics. Degeneracy is accounted for by a factor  $[1-f(E)]$ , where  $f(E)$  is the occupancy of the energy  $E$ . The scattering rate reduction is implemented through a rejection technique as in the case of screened polar-optical interactions.<sup>21</sup> The occupation factor  $f(E)$  is updated at each time step for each of the valleys  $\Gamma$ ,  $L$ , and  $X$ . By counting the number of electrons with an energy in the range  $E$ ,  $E + \Delta E$ , we obtain the energy distribution. To translate this number into the occupation probability, we normalize the number with the density of states. Hence,

$$f_i(E) = \frac{N_i(E)}{\frac{2}{(2\pi)^2} \left[ \frac{2m_i}{\hbar^2} \right]^{3/2} E^{1/2} \Delta E} \frac{n}{N_{\text{elec}}}, \quad (12)$$

where  $N_i(E)$  is the number of electrons in valley  $i$  with energies between  $E$  and  $E + \Delta E$ ,  $n$  is the total concentration, and  $N_{\text{elec}}$  is the number of electrons used in the simulation.

Electron-electron interactions at high carrier concentrations are treated through a molecular-dynamics approach. The Coulombic interaction between electrons is calculated in real space using an Ewald sum technique at each time step.<sup>22</sup> The total Coulombic potential for  $n$  electrons is given by

$$\Phi = \frac{e^2}{4\pi\epsilon(0)} \frac{1}{2} \sum_{i \neq j}^n \frac{1}{r_{ij}}, \quad (13)$$

where  $r_{ij}$  is the distance between electrons  $i$  and  $j$ , and  $n$  is the total number of electrons. Since we are simulating a small volume in the crystal with  $N_{\text{elec}}$  number of electrons, the whole crystal is assumed to be composed of cells which are the exact replicas of this simulated volume. The summation of (13) can be expanded in terms of the cell basis vectors  $\mathbf{L} = L_x \mathbf{a}_x + L_y \mathbf{a}_y + L_z \mathbf{a}_z$  as ( $L_x, L_y, L_z$  are integer multiples of the dimensions of the simulated volume)

$$\Phi = \frac{e^2}{4\pi\epsilon(0)} \frac{1}{2} \sum_{i \neq j}^{N_{\text{elec}}} \frac{1}{r_{ij}} + \sum_{\mathbf{r}; \mathbf{L} > 0} \frac{1}{|\mathbf{L} + \mathbf{r}|}, \quad (14)$$

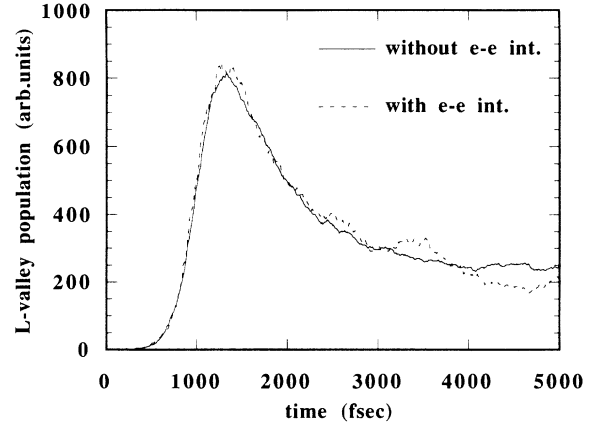


FIG. 3.  $L$ -valley population evolution for  $D_{LX} = 1.5 \times 10^8$  eV/cm. The straight line is for the case with the inclusion of electron-electron Coulomb interactions, the dashed line is for that without.

where the first term is the electron-electron interaction in the cell being simulated, and the second term is due to the replicated cells. For simplicity, only the nearest-neighbor cells are considered in the calculation (minimum image approximation).

The effect of electron-electron Coulomb interactions is seen in the  $L$  valley population evolution and energy distributions of Figs. 3 and 4. Figure 3 illustrates the response of carriers in the  $L$  valley, while Fig. 4 illustrates the distribution functions in the two valleys at 500 fs. There is no appreciable difference in the population evolution curves for the cases with and without the inclusion of electron-electron Coulomb interactions. However, from the population energy distributions in Fig. 4, we see that the  $X$  and  $L$  valley energy distributions are significantly broadened due to electron-electron interactions. These interactions are contributing to the thermalization of the distribution and increasing the number of electrons in the  $X$  valley above the  $X$ - $L$  intervalley

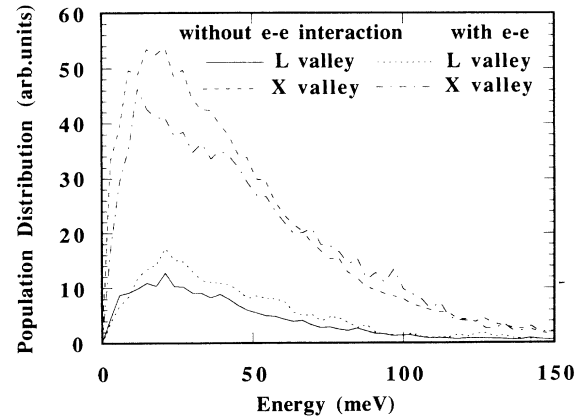


FIG. 4. Energy distribution function of  $X$  and  $L$  valley populations at  $t = 500$  fs after the maximum of the photoexcitation pulse.

scattering threshold (of 66 meV), and also broadening the  $L$  valley distribution so that the scattering rate is higher than the case without the treatment of Coulomb interaction.

### B. EMC simulation of the photogeneration process

The photogeneration process from the valence-band states to the  $X$  and  $L$  conduction bands requires phonon coupling for the indirect-gap semiconductor  $\text{Al}_{0.6}\text{Ga}_{0.4}\text{As}$ . The valence-band states at the  $\Gamma$  point (light- and heavy-hole bands) are composed of the  $p$  states of the group-V elements. The selection rules for phonon coupling depend on the particular path of the generation process. In Fig. 5, the two possible paths for the valence-band to conduction-band transition are shown. In case (i), the valence-band electron absorbs a photon and goes to an intermediate state in the energy gap at the  $\Gamma$  point. The phonon-coupling selection rules for this state are similar to those for  $\Gamma$ - $L$  and  $\Gamma$ - $X$  intervalley scattering, i.e., LO zone-edge phonons are involved in the transition process when the mass of the group-V atom is greater than the III-group atoms. For case (ii), the valence-band electron first couples with a phonon to transfer to an intermediate state in the energy gap, then absorbs a photon for transition into the conduction-band valley. The phonon selection rule for this case is the reverse of case (i), i.e., LA phonons are allowed for the transition to the intermediate state. The absorption rate is given by<sup>16</sup>

$$\Gamma(\hbar\omega_{\text{laser}}) = K \frac{N_{\text{valley}} m^{*3/2}}{\omega_{\text{phonon}}} (N_q + \frac{1}{2} \pm \frac{1}{2}) \times (\hbar\omega_{\text{laser}} - E_{\text{gap}} \mp \hbar\omega_{\text{phonon}})^2, \quad (15)$$

where  $K$  is a constant depending on various material parameters and deformation potentials, but its value is irrelevant in the present case since we already know the total number of photoexcited electrons. The expression in the energy term can be rewritten as

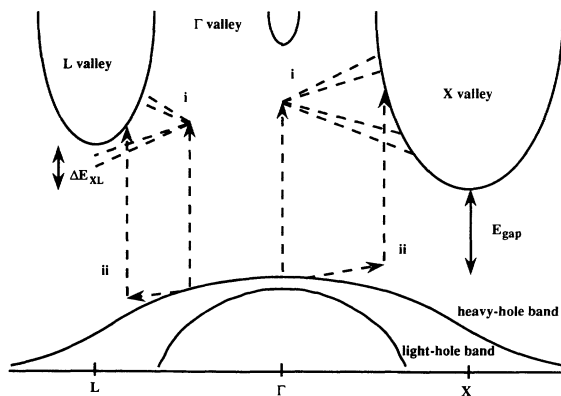


FIG. 5. Photogeneration in indirect-gap  $\text{Al}_x\text{Ga}_{1-x}\text{As}$ . Two generation paths, (i) and (ii), are possible, each with different phonon selection rules.

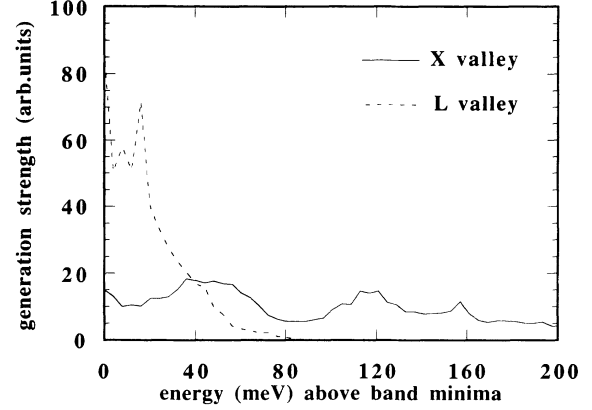


FIG. 6. Photogeneration spectra for the  $X$  and  $L$  valleys assuming equal probabilities for the paths (i) and (ii) in Fig. 5.

$$\hbar\omega_{\text{laser}} - E_{\text{gap}} \mp \hbar\omega_{\text{phonon}} = E_{\text{val}} + E_{\text{cond}} \mp \hbar\omega_{\text{phonon}}, \quad (16)$$

where  $E_{\text{val}}$  and  $E_{\text{cond}}$  are the initial valence-band and final conduction-band energies.

Since the photoexcitation process is complicated by the existence of two sets of LO and LA phonon modes, we need to do a rigorous calculation of the final conduction-band state energies. By using a Monte Carlo approach, the calculation of the initial energies of photoexcited electrons is straightforward. These energies are used in the main EMC route as electrons “appear” through photoexcitation according to a secant hyperbolic squared pulse shape in the program. The method of calculating these energies is as follows: For each electron in the ensemble, a random number decides on the path through which the electron transfers from a valence-band state to the final conduction-band states. The paths are the valence-band state emitting or absorbing an AlAs-like or GaAs-like LO or LA phonon to a final state in the  $X$  or  $L$  bands. The weights of the respective paths are determined from the quantities  $N_{\text{valley}}$ , effective mass  $m^*$  of the conduction band,  $\omega_{\text{phonon}}$ , and the energy expression, in which an initial valence-band energy is chosen randomly with a weight reflecting the density of states in the valence band. This is due to the fact that a wide range of phonon wave vectors can complete the transition. The selected path and initial valence-band energy gives the energy in the  $X$  or  $L$  conduction band. The spectrum of the generated carriers which results from the simulation, assuming equal weights for the paths (i) and (ii) of Fig. 5, is shown in Fig. 6. We can interpret this curve as the absorption spectrum of the semiconductor under continuous-wave illumination. The main simulation is tested for sensitivity to the photogeneration path by alternately assuming path (i) only, path (ii) only, and equal probabilities for both paths of generation. This is discussed in the next section.

### III. RESULTS

The simulations were performed for a range of different values for the intervalley deformation potential  $D_{LX}$ .

These ranged from  $0.5 \times 10^8$  eV/cm to  $5 \times 10^8$  eV/cm. The simulations were also carried out both with and without the band filling, screening of the electron–polar-optical-phonon interaction and Coulombic interaction effects, and for the various photogeneration cases discussed above. A first-order scattering correction to the  $L$ - $X$  intervalley scattering process was also made. However, since the first-order scattering rate is small compared with the zero-order rate, no difference between the simulations for different first-order deformation-potential values (for  $\Xi_0=0, 2.5, 5.0$  eV) was found, indicating that this is an unimportant process.

An important point in interpreting the experimental data of Ref. 12 is the range of  $X$ -valley electron energies at the bottom of the  $X_6$  band which can be probed by the absorption. Since we have different curvatures in the  $X_6$  and  $X_7$  bands, there is a cutoff energy near the bottom of the  $X_6$  band where the electron population is sampled. This energy is given by the expression (under a parabolic-band approximation

$$\Delta E = (E_{\text{probe}} - \Delta E_{X_6-X_7}) \frac{m_{X_7}}{m_{X_6} - m_{X_7}}, \quad (17)$$

where  $\Delta E_{X_6-X_7}$  is the difference between the  $X_6$  and  $X_7$  conduction-band minima,  $m_{X_6}$  and  $m_{X_7}$  are the effective masses in the  $X_6$  and  $X_7$  valleys. The  $X_7$ -valley effective mass is estimated from the band structures of GaAs and AlAs,<sup>23</sup> and interpolating under the virtual-crystal approximation. Using the masses  $m_{X_6}=0.368$  and  $m_{X_7}=0.07$ , and  $\Delta E_{X_6-X_7}=0.3$  eV, we find the cutoff energy  $\Delta E$  to be approximately 20 meV.

In our simulation, we determine the values of the  $X_6$  population lying in the bottom of the band with an energy less than  $\Delta E$ . The resulting curves are convolved with the absorption probe pulsewidth (500 fs FWHM secant hyperbolic squared). The results for  $\Delta E=20$  meV are shown in Fig. 7. We find that a value of  $D_{XL} = 1.5 \pm 0.5 \times 10^8$  eV/cm approximates the evolution

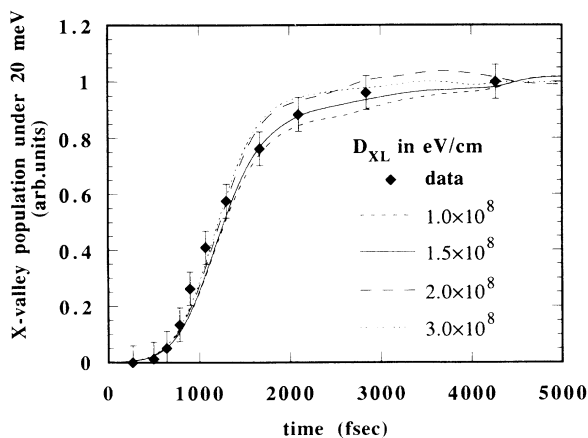


FIG. 7.  $X$ -valley population evolution for different  $L$ - $X$  deformation potentials. The  $X_6$ - $X_7$  transition occurs for  $X_6$ -valley electrons with energy less than  $\Delta E=20$  meV. The photogeneration path (i) is assumed.

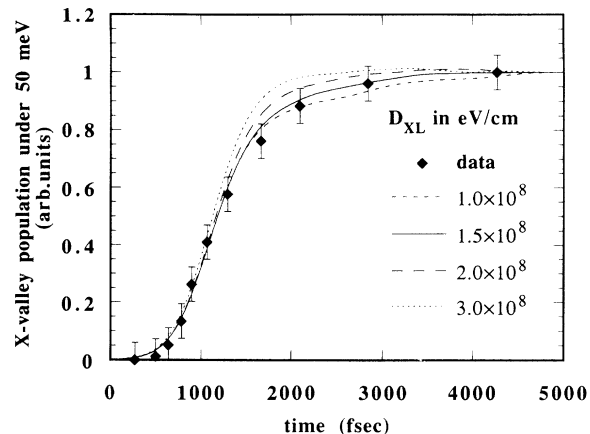


FIG. 8. Same as in Fig. 7, but for a cutoff energy of  $\Delta E=50$  meV for electrons in the bottom of the  $X_6$  valley.

of the  $X$ -valley population with energy less than the probed energy range of 20 meV. For comparison, the corresponding curve of case (i) for  $\Delta E=50$  meV is also given in Fig. 8. In the latter case, the curves lie at larger values than the experimental data at the region where  $L$ - $X$  intervalley scattering is the main mechanism of the  $X$ -valley population increase (i.e., for  $t$  greater than 1500 fs). However, the deformation-potential value  $D_{XL} = 1.5 \times 10^8$  eV/cm is still seen to be good at longer times. The inclusion of effects like band filling, electron–electron interactions, and screened electron–polar-optical-phonon interactions do not have any significant effect on the estimated value of  $D_{XL}$  at an electron concentration of  $2.8 \times 10^{18} \text{ cm}^{-3}$  reported in the experiments of Ref. 12, and the different  $X$ -valley population evolution plots lie within the error bounds of the data. Specifically, the difference between the number of scattering events with and without the inclusion of band filling and polar-optical-phonon screening is less than 3%.

The effect of varying the photogeneration path can be seen in Figs. 9 and 10. In the initial results illustrated in

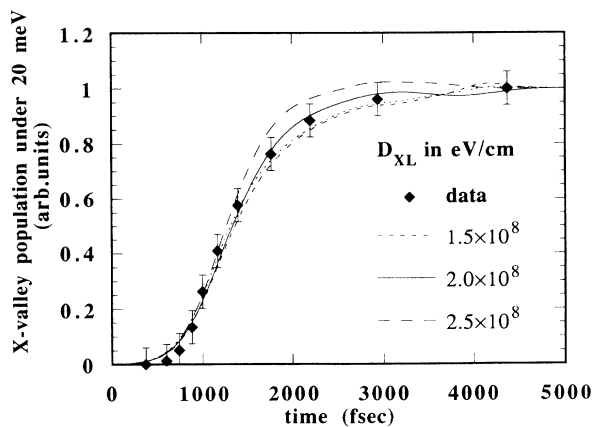


FIG. 9.  $X$ -valley population evolution for electrons with energy less than  $\Delta E=20$  meV, assuming the photogeneration path (ii). Note that the deformation-potential values fitted to the data are higher than in Fig. 7.

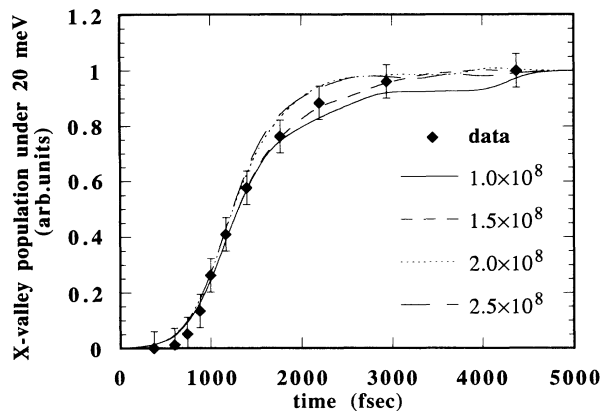


FIG. 10.  $X$ -valley population evolution for electrons with energy less than  $\Delta E = 20$  meV, assuming an equal probability of selection of photogeneration paths (i) and (ii).

Fig. 7, we assumed the photogeneration is due to path (i) only, where only AlAs-like and GaAs-like LO phonons are assumed to couple the intermediate state at the  $\Gamma$  point in the energy gap to the conduction bands. The ratio of photoexcited electrons in the  $L$  valley to those in the  $X$  valley is approximately 0.3. In Fig. 9, photogeneration due to path (ii) is assumed. The ratio of photoexcited electrons in the  $L$  valley to those in the  $X$  valley for this case is approximately 1.1, much larger than the previous case. This mainly occurs because the LA-phonon energies are much smaller than the LO-phonon energies and phonon-emission processes resulting in transfer to the  $L$  valley are more effective. As a result, the  $L$ - $X$  deformation-potential value that fits the data is nearer to  $2.0 \times 10^8$  eV/cm. The results for the case where paths (i) and (ii) are equally probable is shown in Fig. 10. The ratio of photoexcited electrons in the  $L$  valley to those in the  $X$  valley here is approximately 0.6. The deformation potential is clearly somewhere between  $1.5 \times 10^8$  eV/cm and  $2.0 \times 10^8$  eV/cm for this case. Thus, the results we obtain are not particularly sensitive to the details of the photoexcitation process.

The  $L$ - $X$  intervalley scattering lifetime  $\tau_{LX}$  corresponding to  $D_{XL} = 1.5 \times 10^8$  eV/cm is found by keeping a track of the number of  $L$ - $X$  intervalley scattering events. Since the total population of the  $L$  and  $X$  valleys is known, the scattering lifetime is easily found from these numbers as

$$\tau_{LX} = - \frac{\Delta t}{\ln \left( \frac{N_L - N_{\text{scat}}}{N_L} \right)}, \quad (18)$$

where  $N_{\text{scat}}$  is the number of scattering events that occur in a period  $\Delta t$ , and  $N_L$  is the initial  $L$ -valley population at the beginning of the time period considered. For the case without the electron-electron interaction,  $\tau_{LX} = 700 \pm 100$

fs; and with the electron-electron interaction we find  $\tau_{LX} = 600 \pm 100$  fs. These values are a factor of 3 to 4 larger than the scattering lifetimes derived through the rate equation analysis of Ref. 12, which calculated a  $\tau_{LX} = 200 \pm 100$  fs lifetime. The intervalley deformation-potential value reported in Ref. 12,  $D_{XL} = 3 \times 10^8$  eV/cm, is also a factor of 2 greater than our results. However, from the definition of the deformation potential describing the interaction between a single-phonon mode and electrons, the value of  $D_{LX}$  is partitioned between the two LO-phonon modes, thereby being a factor of  $\sqrt{2}$  smaller than an assumption of a single effective phonon mode as in Ref. 12.

#### IV. CONCLUSION AND DISCUSSION

The photogeneration process and hot-carrier relaxation in femtosecond photoexcited indirect-gap  $\text{Al}_x\text{Ga}_{1-x}\text{As}$  was studied using an ensemble Monte Carlo simulation technique. High-density effects such as screening of the polar-optical-phonon interaction, band filling, and electron-electron Coulomb interaction were also included in the simulation. The effects of these corrections were not distinguishable within the error bars of the experimental data. The sensitivity of the simulation to the photogeneration process, and also the relatively small cutoff energy of sampling of the  $X_6$ -valley population in the infrared-absorption data were, on the other hand, checked carefully. The calculation of exact probabilities of the photogeneration paths of Fig. 5 are complicated by the fact that the phonon selection rules are not strict in the random alloy. Similarly, the intervalley phonon scattering process is also affected by alloy randomness and symmetry breaking. Another possibly important alloy effect, alloy-assisted elastic intervalley transitions,<sup>24,25</sup> was not considered in this simulation, the effect of which would decrease the intervalley deformation-potential value derived by phonon-assisted intervalley scattering processes only. However, by comparing with the  $L$ - $X$  scattering deformation potentials for AlAs and GaAs of Ref. 11, a value of  $D_{LX} = 2.4 \times 10^8$  eV/cm is found from the empirical-pseudopotential calculations. Considering the fact that our definition of the deformation potential also includes the fact that there are two alloy phonon modes, this value (divided by  $\sqrt{2}$  to be applicable to our definition where the scattering due to two phonon modes is treated as separate scattering processes) is close to our result. The value we conclude is appropriate for the electron-phonon coupling constant for intervalley scattering between the  $X$  and  $L$  valleys is  $1.7 \pm 0.5 \times 10^8$  eV/cm.

#### ACKNOWLEDGMENT

This work was supported by the Office of Naval Research.

- <sup>1</sup>J. Shah, B. Deveaud, T. C. Damen, W. T. Tsang, A. C. Gosard, and P. Lugli, *Phys. Rev. Lett.* **59**, 2222 (1987).
- <sup>2</sup>W. Hackenberg and G. Fasol, *Solid-State Electron.* **32**, 1247 (1989).
- <sup>3</sup>G. Fasol, W. Hackenberg, H. P. Hughes, K. Ploog, E. Bauser, and H. Kano, *Phys. Rev. B* **41**, 1461 (1990).
- <sup>4</sup>R. G. Ulbrich, J. A. Kash, and J. C. Tsang, *Phys. Rev. Lett.* **62**, 949 (1989).
- <sup>5</sup>W. B. Wang, N. Ockman, M. Yan, and R. R. Alfano, *Solid-State Electron.* **32**, 1337 (1989).
- <sup>6</sup>R. Mickevicius and A. Reklaitis, *Semicond. Sci. Technol.* **5**, 805 (1990).
- <sup>7</sup>J. Pozhela and A. Reklaitis, *Solid-State Electron.* **23**, 927 (1980).
- <sup>8</sup>M. A. Littlejohn, J. R. Hauser, and T. H. Glisson, *J. Appl. Phys.* **48**, 4587 (1977).
- <sup>9</sup>P. Lugli and D. K. Ferry, *Phys. Rev. Lett.* **56**, 1295 (1986).
- <sup>10</sup>S. E. Günçer and D. K. Ferry, *Semicond. Sci. Technol.* **7**, 8324 (1992).
- <sup>11</sup>S. Zollner, S. Gopalan, and M. Cardona, *J. Appl. Phys.* **68**, 1682 (1990).
- <sup>12</sup>W. B. Wang, K. Shum, R. R. Alfano, D. Szymd, and A. J. Nozik, *Phys. Rev. Lett.* **68**, 662 (1991).
- <sup>13</sup>M. J. Kann, A. M. Krizan, and D. K. Ferry, *Phys. Rev. B* **41**, 12 659 (1990).
- <sup>14</sup>S. Adachi, *J. Appl. Phys.* **58**, R1 (1985).
- <sup>15</sup>M. Teicher, R. Beserman, M. V. Klein, and H. Morkoç, *Phys. Rev. B* **29**, 4652 (1984).
- <sup>16</sup>D. K. Ferry, *Semiconductors* (MacMillan, New York, 1991).
- <sup>17</sup>B. K. Ridley, *Quantum Processes in Semiconductors* (Clarendon, Oxford, 1988).
- <sup>18</sup>D. K. Ferry, *J. Appl. Phys.* **50**, 1422 (1979).
- <sup>19</sup>P. Lugli, C. Jacoboni, L. Reggiani, and P. Kocevar, *Appl. Phys. Lett.* **50**, 1251 (1987).
- <sup>20</sup>M. A. Osman and D. K. Ferry, *Phys. Rev. B* **36**, 6018 (1987).
- <sup>21</sup>P. Lugli and D. K. Ferry, *IEEE Trans. Electron Devices* **32**, 2431 (1985).
- <sup>22</sup>M. J. Kann, A. M. Krizan, and D. K. Ferry, *Solid-State Electron.* **32**, 1831 (1989).
- <sup>23</sup>A. B. Chen, and A. Sher, *Phys. Rev. B* **23**, 5360 (1981).
- <sup>24</sup>H. Kalt, W. W. Rühle, and K. Reimann, *Solid-State Electron.* **32**, 1819 (1989).
- <sup>25</sup>C. H. Grein, S. Zollner, and M. Cardona, *Phys. Rev. B* **44**, 12 761 (1991).